

## Light-Driven Extremely Nonlinear Bulk Photogalvanic Currents

Ofer Neufeld<sup>1,\*</sup>, Nicolas Tancogne-Dejean<sup>1</sup>, Umberto De Giovannini<sup>1,2,4</sup>

Hannes Hübener<sup>1</sup> and Angel Rubio<sup>1,3,4,†</sup>

<sup>1</sup>Max Planck Institute for the Structure and Dynamics of Matter and Center for Free-Electron Laser Science, Hamburg 22761, Germany

<sup>2</sup>IKERBASQUE, Basque Foundation for Science, E-48011 Bilbao, Spain

<sup>3</sup>Center for Computational Quantum Physics (CCQ), The Flatiron Institute, New York, New York 10010, USA

<sup>4</sup>Nano-Bio Spectroscopy Group, Universidad del País Vasco UPV/EHU, 20018 San Sebastián, Spain



(Received 2 May 2021; accepted 28 July 2021; published 13 September 2021)

We predict the generation of bulk photocurrents in materials driven by bichromatic fields that are circularly polarized and corotating. The nonlinear photocurrents have a fully controllable directionality and amplitude without requiring carrier-envelope-phase stabilization or few-cycle pulses, and can be generated with photon energies much smaller than the band gap (reducing heating in the photoconversion process). We demonstrate with *ab initio* calculations that the photocurrent generation mechanism is universal and arises in gaped materials (Si, diamond, MgO, hBN), in semimetals (graphene), and in two- and three-dimensional systems. Photocurrents are shown to rely on sub-laser-cycle asymmetries in the nonlinear response that build-up coherently from cycle to cycle as the conduction band is populated. Importantly, the photocurrents are always transverse to the major axis of the co-circular lasers regardless of the material's structure and orientation (analogously to a Hall current), which we find originates from a generalized time-reversal symmetry in the driven system. At high laser powers ( $\sim 10^{13}$  W/cm<sup>2</sup>) this symmetry can be spontaneously broken by vast electronic excitations, which is accompanied by an onset of carrier-envelope-phase sensitivity and ultrafast many-body effects. Our results are directly applicable for efficient light-driven control of electronics, and for enhancing sub-band-gap bulk photogalvanic effects.

DOI: [10.1103/PhysRevLett.127.126601](https://doi.org/10.1103/PhysRevLett.127.126601)

Light-driven dynamics in solids with femtosecond time-scales have recently attracted considerable attention. Light-matter interactions can result in novel effects that originate from ultrafast dynamics including high harmonic generation (HHG) [1], and the creation of new states of matter [2–10]. The ability to control the electron motion in real space, momentum space, and time, can give rise to unprecedented control over observable properties such as light emission [11–19] and magnetic fields [20]. One main avenue of research here is the generation and characterization of light-driven bulk electric currents in the absence of external bias. In materials with broken inversion symmetry, second-order nonlinear effects lead to shift currents through the bulk photovoltaic effect [21,22]. The driving force for carrier separation in the shift current mechanism is the coherent evolution of electron and hole wave functions, such that above-band-gap photovoltages can surpass the Shockley-Queisser limit [23]. Photocurrents can also arise

in inversion-symmetric materials (where they are standardly forbidden) via mixing of bichromatic carrier waves with frequencies  $\omega$  and  $2\omega$  [20,24–28]. Here the photon energies are resonant with perturbative transitions that interfere, and the inversion symmetry is effectively broken by the two-color field (making the effect highly sensitive to the two-color relative phase). The resonant and perturbative nature of these effects precludes access to ultrafast dynamics and possible applications in the terahertz regime, and is also limited in its conversion efficiency [29].

More recently, nonlinear photocurrents driven by intense quasi-monochromatic few-cycle pulses were predicted and observed in dielectrics [30–32] and graphene [33–36]. The microscopic mechanism creating these photocurrents relies on the vector potential of the light field having a nonzero time integral [32]; i.e., there are residual direct terms that only exist in few-cycle pulses. Consequently, these photocurrents are highly sensitive to the carrier-envelope-phase (CEP) and cancel out in non-CEP-stabilized conditions. Controlling or utilizing such currents for ultrafast spectroscopy is challenging, and their applications for energy conversion remains elusive.

Here we explore strong-field driven photocurrents with  $\omega - 2\omega$  lasers that are circularly polarized and corotating (Fig. 1). We show that in this regime bulk photocurrents are

Published by the American Physical Society under the terms of the [Creative Commons Attribution 4.0 International](https://creativecommons.org/licenses/by/4.0/) license. Further distribution of this work must maintain attribution to the author(s) and the published article's title, journal citation, and DOI. Open access publication funded by the Max Planck Society.

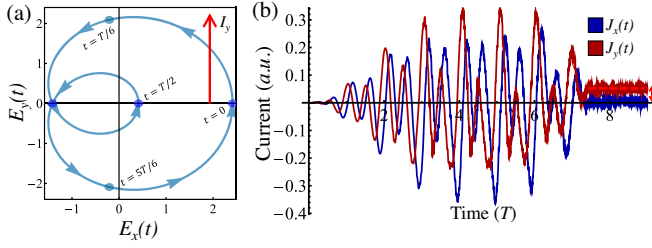


FIG. 1. Bulk photocurrent generation in diamond by THz cocircular  $\omega - 2\omega$  fields. (a) Schematic Lissajous curve for the time-dependent polarization of the field in Eq. (1) (for  $\phi = 0$ ,  $\Delta = \sqrt{2}$ ). Small arrows indicate the direction of time, and the red arrow indicates the direction of the photocurrent ( $I$ ). Different instances in time are highlighted to emphasize the mirror symmetry of the Lissajous about its  $x$  axis, but not the  $y$  axis. (b) Calculated current expectation value (see Supplemental Material [37] for details) for laser field polarized in the (111) planes (with  $\lambda = 2500$  nm,  $\phi = 0$ ,  $\Delta = \sqrt{2}$ ,  $I_0 = 7.5 \times 10^{12}$  W/cm $^2$ ). The current is given in  $10^{-3}$  atomic units.

produced with several attractive features: (i) they do not require CEP stabilized few-cycle pulses, (ii) they do not require resonant or near-resonant transitions, (iii) their amplitude is insensitive to the two-color phase and is finely tunable, (iv) their directionality is controlled by the two-color phase regardless of the material system. The photocurrents are shown to arise from excited-state occupation imbalances in the Brillouin zone (BZ) that build-up from cycle-to-cycle, and analogously to anomalous Hall currents [9] are always transverse to the main axis of the two-color field. However, in contrast to anomalous Hall currents they do not require bias or magnetic fields. We explain the origin of this effect intuitively based on sub-cycle electron dynamics, and by a generalized time-reversal symmetry in the laser-dressed system. Lastly, we show that for higher laser powers the generalized time-reversal symmetry is spontaneously broken by vast excitations to the conduction band (CB) that cause a breakdown of the independent-particle approximation (IPA), and also lead to CEP sensitivity. These results should be useful for all-optical ultrafast control of electron dynamics, for energy conversion with sub-band-gap light in bulk and spatially uniform materials, and for developing novel ultrafast spectroscopy techniques based on nonlinear photocurrents.

We begin by introducing the  $\omega - 2\omega$  laser that comprises two corotating circularly polarized beams:

$$\mathbf{E}(t) = \frac{E_0}{\sqrt{2}} f(t) \text{Re}\{ (e^{i\omega t} + \Delta e^{2i\omega t + \phi}) \hat{e}_+ \}, \quad (1)$$

where  $E_0$  is the electric field amplitude of the  $\omega$  beam taken here in the range of 0.085–0.85 V/Å (equivalent to powers of  $\sim 10^{11}$ – $10^{13}$  W/cm $^2$ ),  $f(t)$  is a dimensionless envelope function (see Supplemental Material [37] for details),  $\omega$  is the fundamental frequency,  $\phi$  is the  $\omega - 2\omega$  relative phase,

$\Delta$  is the beams' amplitude ratio, and  $\hat{e}_+$  is a right circularly polarized unit vector. Note that we have employed the dipole approximation, which is valid in our wavelength ranges. A representative Lissajous curve for the time-dependent polarization of this field is presented in Fig. 1(a). Its main characteristic features are (i) it exhibits a mirror symmetry along its  $x$  axis, (ii) the field peak power and time-dependent polarization substantially differ along the positive and negative ends of the  $x$  axis, i.e., at the start and middle of an optical cycle where the two fields constructively or destructively interfere [corresponding to  $t = 0$  and  $t = T/2$ , respectively, see Fig. 1(a)]. Importantly, the direction of the field's mirror axis and its spatiotemporal structure is CEP independent and only depends on  $\phi$ . The interaction of  $\mathbf{E}(t)$  in Eq. (1) with matter is described from first principles with time-dependent density functional theory (TDDFT) within the adiabatic local density approximation (LDA) in the real-space code octopus [38–40] (core levels are replaced by appropriate norm-conserving pseudopotentials [41]), with which the time-dependent electronic current expectation value,  $\mathbf{J}(t)$ , is calculated (all technical details are delegated to the Supplemental Material [37]).

As a starting point, we analyze driven electron dynamics in diamond subject to  $\mathbf{E}(t)$  in Eq. (1). Diamond represents a benchmark system since it has a simple lattice structure and is a wide band gap insulator with an indirect gap of 5.48 eV and a direct gap at the  $\Gamma$  point of 7.3 eV [42,43]. These points easily allow extensive calculations with wavelengths well below the band gap (within the LDA the direct gap is 5.65 eV, slightly lower than the experimental value). Figure 1(b) presents the calculated current, where  $\mathbf{E}(t)$  is polarized in the diamond (111) planes and is comprised of 2500–1250 nm light in the strong-field regime ( $I_0 = 7.5 \times 10^{12}$  W/cm $^2$ ). A residual photocurrent is observed along the  $y$  axis after the laser pulse ends (axes are denoted with respect to the field's coordinate system), which is experimentally detectable using existing methods (see, for instance, Refs. [25,27,28,30,32–34]). This effect cannot result from CEP sensitivity since the pulse has a long duration with a zero time-integral over the vector potential. Moreover, the driving frequencies are much below the band gap—it would take over 11  $\omega$  photons to induce a transition from the valence band (VB) to the CB. Thus, this effect substantially differs from previously discussed perturbative and/or resonant phenomena [24–28]. We note that the current generally arises from contributions of both electrons and holes that do not cancel. Importantly, it also does not decay in our simulation [see Fig. 1(b)]. This is true even in the presence of electron-electron interactions incorporated in the simulation, indicating that electrons occupy a true excited state of the system [similar behavior occurs with a Perdew-Burke-Ernzerhof (PBE) functional [44], see Supplemental Material [37]]. The current is thus only expected to decay due to scattering channels not included in our model [45].

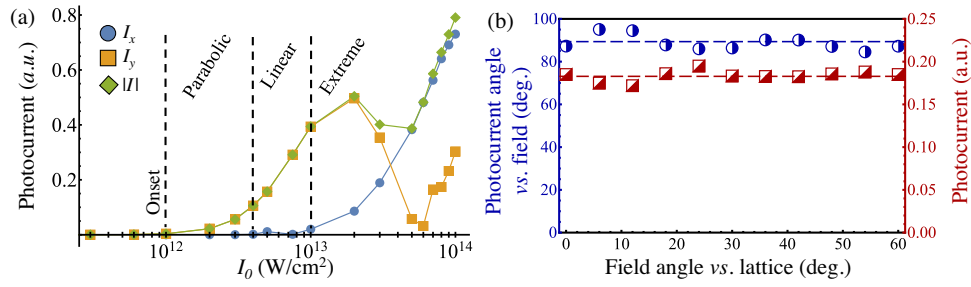


FIG. 2. Numerical investigation of nonlinear photocurrents in diamond. (a) Photocurrent amplitude vs the field power (for  $\lambda = 1200$  nm,  $\phi = 0$ ,  $\Delta = \sqrt{2}$ ). The plot is partitioned to different regimes as indicated by dashed lines.  $I_0$  is given in logarithmic scale. (b) Photocurrent direction in the (111) planes with respect to the field’s  $x$  axis (blue) and photocurrent amplitude (red) vs the field’s orientation with respect to the lattice (for  $\lambda = 1200$  nm,  $\Delta = 1$ ,  $I_0 = 7.5 \times 10^{12}$  W/cm<sup>2</sup>). The current is given in  $10^{-3}$  atomic units.

To understand the mechanism behind this effect we explore its dependence on the various laser parameters. Figure 2(a) presents the calculated photocurrent amplitude vs the applied laser power,  $I_0$ , which multiplies both the  $\omega$  and  $2\omega$  components. As expected, the current originates from nonlinear interactions—there is an onset at  $I_0 = 10^{12}$  W/cm<sup>2</sup> which initially increases parabolically with  $I_0$ , indicating that the current is proportional to four-photon processes in the perturbative regime. Indeed, four photons are the minimal number to traverse the band gap for this wavelength (1200 nm) while still mixing both photon types (corresponding to annihilation of three  $2\omega$  photons and one  $\omega$  photon, or two  $2\omega$  photons and two  $\omega$  photons). This mixing is crucial since without it there is no symmetry breaking as in Fig. 1(a) that allows photocurrents to be created (because the individual field components are circularly polarized with no preferential direction in space).

For powers above  $I_0 \approx 5 \times 10^{12}$  W/cm<sup>2</sup> (and Keldysh parameters in ranges 1-2 for the  $\omega$  field) in Fig. 2(a) the parabolic behavior changes to linear proportionality to  $I_0$ , paradoxically suggesting that two-photon processes are dominant. Since two photons cannot promote electrons to the CB, higher nonlinear effects are at play. Further increasing the power changes this behavior to an unpredictable pattern that also induces nonzero  $x$ -polarized currents. We will explore this behavior in detail below, but first we explain the origin of the photocurrent in the intermediate strong-field regime (for  $10^{12} < I_0 < 10^{13}$  W/cm<sup>2</sup>). Figure 2(b) presents the current direction vs the orientation of the major axis of  $\mathbf{E}(t)$  in the (111) planes. The photocurrent remains transverse to the  $x$  axis defined by the Lissajous in Fig. 1(a). This is despite the different local lattice symmetries that are probed as the field rotates (e.g., breaking local reflection or rotational symmetries). Figure 2(b) further shows that throughout this control, the current maintains its amplitude and only exhibits mild modulations. Similar results are obtained when  $\mathbf{E}(t)$  is polarized in the (110) planes that have a different local symmetry (fourfold rather than sixfold, see Supplemental Material [37]). These features thus seem

analogous to those of anomalous Hall currents, though notably here the laser field has components along both and directions—it is just the main mirror axis of the Lissajous that dictates the direction of the photocurrent.

Figures 3(a) and 3(b) present the integrated and normalized electron occupations in the CB after the laser pulse ends. That is, it shows the occupations along  $k'_x$ ,  $k'_y$ ,  $k'_z$  axes in  $k$  space after integrating over the other two axes (see Supplemental Material [37] for details). Note that the “prime” coordinate system denotes the diamond primitive unit cell coordinates rather than those of the Lissajous, thus a current along the  $y$  axis of the field is expected to show up as imbalances in occupations along all three  $k'_x$ ,  $k'_y$ ,  $k'_z$  axes. The occupations around the  $\Gamma$  point are asymmetric—electron occupations break the inversion symmetry in  $k$  space, which is generally a consequence of time-reversal symmetry. Since  $\mathbf{E}(t)$  breaks time-reversal symmetry,  $k$ -inversion symmetry is broken as well, allowing photocurrents to be generated. We also note that almost all  $k$  points in the BZ contribute to this asymmetry, even far away from the  $\Gamma$  point.

To understand why photocurrent components parallel to the  $x$  axis are not generated, we analyze the dynamics of electrons driven in the strong-field regime assuming that the current is generated by two sequential steps: (i) First, the strong field excites an electron from the VB to the CB (through Landau-Zener transitions). This step is most likely to occur near the field peak power and near the minimal band gap [see highlighted points in Fig. 1(a)]. (ii) Second, the excited electron is driven in the CB by the laser, generating intraband currents and occupying different regions in the BZ. Since the Lissajous in Fig. 1(a) is symmetric about its  $x$  axis, one expects an equivalent occupation of states with positive or negative  $k_y$  to form during the acceleration in step (ii). However, because the events that initiate tunneling are very different, a discrepancy is formed in step (i)—trajectories that are initiated for positive  $k_y$  are favorable, leading to a residual current. Since no such discrepancies exists along the  $y$  axis of the field [e.g., at  $t = T/6$  and  $t = 5T/6$ , see Fig. 1(a)], no

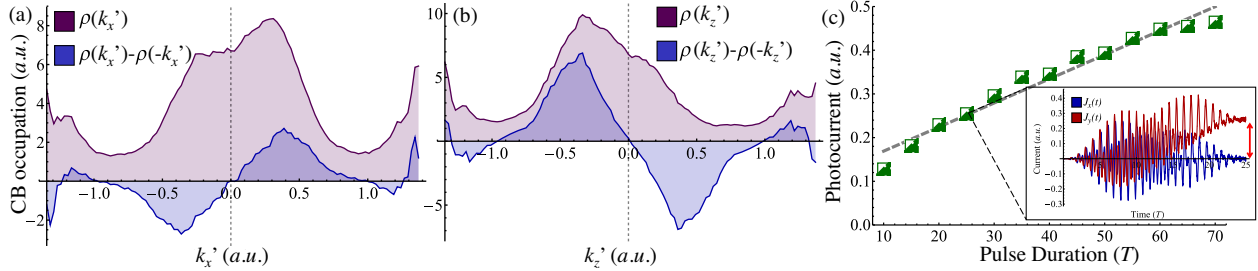


FIG. 3. Conduction band occupations in diamond after interaction with  $\omega - 2\omega$  cocircular laser, and photocurrent proportionality to the pulse duration. (a),(b) CB occupations (denoted by  $\rho$ ) along  $k'_x$  and  $k'_z$  axes, respectively, integrated over the other two axes, presented in the coordinate system of the lattice ( $k'_y$  is not shown due to similarity to  $k'_x$ ).  $\rho$  is normalized to the density of states,  $g(k')$ . Purple curves show the CB occupation, while blue curves show the deviation from inversion symmetry (i.e., the occupations subtracted from their inverted image), indicating which states contribute to the photocurrent. Calculated for  $\lambda = 1200$  nm,  $\phi = 0$ ,  $\Delta = \sqrt{3}$ ,  $I_0 = 7.5 \times 10^{12}$  W/cm $^2$ . (c) Photocurrent amplitude vs pulse duration. Inset shows calculation for a 25-cycle pulse showing the build-up of photocurrent from cycle to cycle. Calculated for the same parameters as (a) except  $\Delta = \sqrt{2}$ . The current is given in  $10^{-3}$  atomic units.

imbalance is generated along the  $k_x$  axis. Overall, through Landau-Zenner transitions in step (i) the asymmetry of the  $\omega - 2\omega$  field is effectively imprinted onto the occupations in the BZ, allowing photocurrent generation.

A different explanation for this effect follows from the analysis of the spatiotemporal symmetries of  $\mathbf{E}(t)$  [46]. Because of its mirror axis [see Fig. 1(a)],  $\mathbf{E}(t)$  is invariant under a coupled operation of time-reversal accompanied by a reflection of its  $y$  polarization:  $\mathbf{E}(t) = \sigma_x \times \mathbf{E}(-t)$  (here  $\sigma_x$  denotes a reflection  $E_y \rightarrow -E_y$ ). Since for  $k$ -space occupations time reversal is equivalent to inversion, this symmetry dictates a mirror plane along the  $k_{yz}$  plane. That is, occupations must be symmetric for  $k_x \rightarrow -k_x$  due to a generalized time reversal exhibited by the field, forbidding  $x$ -polarized photocurrents (note that  $x$  labels the coordinate system of the field). We note that this analysis is formally valid only if neglecting other effects that may lead to symmetry breaking, e.g., the finite pulse duration or the local lattice structure. Nevertheless, the numerical results are consistent with this conclusion for a wide parameter range and different materials. This indicates that in this regime the spatio-temporal structure of the laser field is crucial.

Figure 3(c) shows the calculated photocurrent amplitudes for different pulse durations for a fixed laser power. The current increases linearly with the pulse duration—asymmetries in  $k$ -space occupations build up coherently from cycle to cycle, allowing a finely-tuned control over the current and emphasizing the importance of subcycle dynamics.

Having established the main results in diamond, we explore other systems (most results are delegated to the Supplemental Material [37] for brevity). First, we show that similar effects arise in silicon, a common photovoltaic energy conversion material [47] [see Fig. S4(a) in the Supplemental Material [37]]. Second, we show that nonlinear photocurrents arise also in MgO [see Fig. S4(b) [37]], which is a wide band gap oxide with primarily ionic

bonding. Hence, the current generation is largely independent of the solid's characteristics. Third, we investigate a monolayer of hBN subject to  $\mathbf{E}(t)$ , showing that similar photocurrents arise (see Fig. S5 [37]). We note that this result differs from the one obtained with a counterrotating bicircular field that does not generate photocurrents [19,48]. Lastly, we explore driven electron dynamics in graphene, where interactions are resonant. Nonetheless, photocurrents arise just as has been shown experimentally for the few-cycle case [33,34], but with stronger asymmetries in CB occupations (see Fig. S6 [37]). Remarkably, the K and K' points in the BZ are still connected by the generalized time-reversal symmetry, such that their total integrated occupations are identical, but the occupation patterns allow nonzero photocurrents.

Finally, we discuss the extreme regime for  $I_0 > 10^{13}$  W/cm $^2$  (which is experimentally accessible) in diamond [Fig. 2(a)]. Here  $x$ -polarized photocurrents are also allowed. Moreover, the current increase vs  $I_0$  is erratic and indicative of highly nonlinear effects. We find that several phenomena occur that contribute to this behavior and result from spontaneous symmetry breaking to the generalized time-reversal symmetry (that forbids the  $x$ -polarized currents for  $I_0 < 10^{13}$  W/cm $^2$ ). In this regime the excitation from the first VB to the CB is so fast and vast that the VB maxima at the  $\Gamma$  point is largely depleted even before the laser pulse ends [see Fig. 4(a)]. Thus, as the system evolves electrons must traverse larger gaps that are contributed from farther  $k$  points, which breaks time-reversal symmetry. Intuitively, this leads to a subcycle asymmetry that allows  $x$ -polarized photocurrents, since occupations in the first half of an optical cycle no longer exactly cancel with those in the second half. In an extreme case, the VB may be fully depleted in a single half-cycle, resulting in very large  $x$ -photocurrents. We note that it is unclear if all, or just some, of these effects are observable below the material

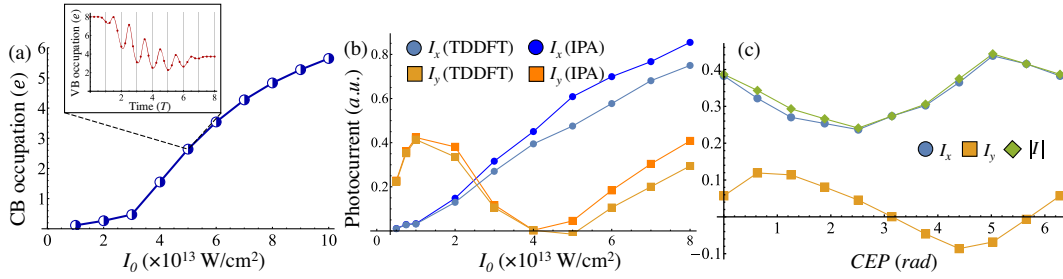


FIG. 4. Spontaneous symmetry breaking in extremely nonlinear photocurrents in diamond. (a) Total excitation of electrons to the CB per primitive cell vs  $I_0$ . Inset shows the electron occupation on the VBs during interaction with the laser pulse for the exemplary case of  $I_0 = 5 \times 10^{13}$  W/cm $^2$ , showing that the VB is quickly depopulated even during the turn-on of the laser pulse. (b) Deviation in photocurrent amplitudes between the IPA and the TDDFT calculation vs field power (for  $\lambda = 1200$  nm,  $\phi = 0$ ,  $\Delta = \sqrt{3}$ ,  $I_0 = 5 \times 10^{13}$  W/cm $^2$ ). (c) Calculated photocurrent amplitudes vs CEP, showing that CEP sensitivity arises in the extremely strong-field regime. Calculated for the same parameters as (a), except with  $\Delta = \sqrt{2}$ . The current is given in  $10^{-3}$  atomic units.

damage threshold (which can be manipulated by changing the laser parameters or the material).

Besides the onset of  $x$ -polarized photocurrents, two other effects come into play. First, dynamical electron-electron interactions play a major role. The excitation of many electrons to the CB significantly renormalizes the effective exchange and correlation interactions from cycle-to-cycle. Figure 4(b) shows photocurrent amplitudes calculated by two different levels of theory—either freezing or not the Hartree and exchange-correlation (HXC) potentials to their ground-state form (the frozen HXC approximation is equivalent to the IPA). Discrepancies between these theories only arise due to the inclusion of electron-electron interactions induced by the laser, and are usually very small [49–54]. Below  $10^{13}$  W/cm $^2$  these are negligible (<5%). Above  $10^{13}$  W/cm $^2$  there are significant deviations in the obtained photocurrent [ $>20\%$ , see Fig. 4(b)], as well as in the intensity of harmonic emission ( $>50\%$ , see Fig. S3 in the Supplemental Material [37]). The deviations increase with field strength, in accordance with the CB population [e.g., compare Fig. 4(a) to 4(b)]. We note that it is not yet clear whether this effect is well described within adiabatic TDDFT, thus results could be affected by the level of theory describing electron-electron interactions. Second, otherwise negligible envelope effects become significant. Figure 4(c) presents the photocurrent amplitudes in this regime vs the CEP, showing that there is strong CEP sensitivity even though the pulse durations are long, and no such sensitivity is observed for weaker power (see Supplemental Material [37] Fig. S2). Both of these phenomena could be probed by measuring the photocurrent and its direction in space.

To summarize, we investigated the interaction of solids with bichromatic  $\omega - 2\omega$  lasers with co-rotating circularly polarized components. We showed that photocurrents are generated in the bulk without external bias due to a coherent excitation of electrons to the CB that builds up from cycle to cycle. A generalized time-reversal symmetry exhibited in

the system imposes that only transverse photocurrents are generated, allowing ideal control over the current amplitude and directionality. This effect is general to three- and two-dimensional systems, gapped insulators, semimetals, and does not strongly depend on the material properties. We also analyzed an extreme strong-field regime where time reversal is spontaneously broken, leading to ultrafast laser-induced correlations, as well as CEP sensitivity from long pulses. Both these phenomena pave the way to novel forms of ultrafast spectroscopy for electron dynamics that rely on nonlinear photocurrents. We note that we analyzed here photocurrent generation from a microscopic standpoint that assumes that the bi-chromatic field components are phase matched. However, phase mismatch in thick media could alter the current’s direction in space which may provide additional control, or could be suppressed by the material and laser parameter choice. From a theoretical standpoint, our work outlines the validity domains of simpler theoretical approaches that rely on the IPA. Notably, we focused here on light materials with weak spin-orbit coupling, but using heavier elements might allow a similar control of spin-polarized bulk currents (because the driving lasers are circularly polarized). Importantly, our results demonstrate a method for sub-band-gap bulk photovoltaic energy conversion that is not bounded by any theoretical limit. Looking forward, these ideas could also be employed to enhance photogalvanic effects in perovskites [22], and for improved control in petahertz electronics [55].

We thank Dr. Shunsuke A. Sato for helpful discussions. We acknowledge financial support from the European Research Council (ERC-2015-AdG-694097), by the Cluster of Excellence “Advanced Imaging of Matter” (AIM), Grupos Consolidados (IT1249-19) and SFB925 “Light induced dynamics and control of correlated quantum systems.” The Flatiron Institute is a division of the Simons Foundation. O. N. gratefully acknowledges the support of the Humboldt Foundation.

\*Corresponding author.  
ofer.neufeld@gmail.com  
†Corresponding author.  
angel.rubio@mpsd.mpg.de

- [1] S. Ghimire and D. A. Reis, High-harmonic generation from solids, *Nat. Phys.* **15**, 10 (2019).
- [2] N. H. Lindner, G. Refael, and V. Galitski, Floquet topological insulator in semiconductor quantum wells, *Nat. Phys.* **7**, 490 (2011).
- [3] Y. H. Wang, H. Steinberg, P. Jarillo-Herrero, and N. Gedik, Observation of Floquet-Bloch states on the surface of a topological insulator, *Science* **342**, 453 (2013).
- [4] A. G. Grushin, Á. Gómez-León, and T. Neupert, Floquet Fractional Chern Insulators, *Phys. Rev. Lett.* **112**, 156801 (2014).
- [5] P. Titum, N. H. Lindner, M. C. Rechtsman, and G. Refael, Disorder-Induced Floquet Topological Insulators, *Phys. Rev. Lett.* **114**, 056801 (2015).
- [6] H. Hübener, M. A. Sentef, U. De Giovannini, A. F. Kemper, and A. Rubio, Creating stable Floquet-Weyl semimetals by laser-driving of 3D dirac materials, *Nat. Commun.* **8**, 13940 (2017).
- [7] H. Hübener, U. De Giovannini, and A. Rubio, Phonon driven Floquet matter, *Nano Lett.* **18**, 1535 (2018).
- [8] G. E. Topp, G. Jotzu, J. W. McIver, L. Xian, A. Rubio, and M. A. Sentef, Topological Floquet engineering of twisted bilayer graphene, *Phys. Rev. Research* **1**, 023031 (2019).
- [9] J. W. McIver, B. Schulte, F.-U. Stein, T. Matsuyama, G. Jotzu, G. Meier, and A. Cavalleri, Light-induced anomalous Hall effect in graphene, *Nat. Phys.* **16**, 38 (2020).
- [10] M. Buzzi *et al.*, Photomolecular High-Temperature Superconductivity, *Phys. Rev. X* **10**, 031028 (2020).
- [11] M. Schultze, E. M. Bothschafter, A. Sommer, S. Holzner, W. Schweinberger, M. Fiess, M. Hofstetter, R. Kienberger, V. Apalkov, V. S. Yakovlev, M. I. Stockman, and F. Krausz, Controlling dielectrics with the electric field of light, *Nature (London)* **493**, 75 (2013).
- [12] O. Schubert, M. Hohenleutner, F. Langer, B. Urbanek, C. Lange, U. Huttner, D. Golde, T. Meier, M. Kira, S. W. Koch, and R. Huber, Sub-cycle control of terahertz high-harmonic generation by dynamical Bloch oscillations, *Nat. Photonics* **8**, 119 (2014).
- [13] H. Liu, Y. Li, Y. S. You, S. Ghimire, T. F. Heinz, and D. A. Reis, High-harmonic generation from an atomically thin semiconductor, *Nat. Phys.* **13**, 262 (2017).
- [14] Y. S. You, D. A. Reis, and S. Ghimire, Anisotropic high-harmonic generation in bulk crystals, *Nat. Phys.* **13**, 345 (2017).
- [15] T. T. Luu and H. J. Wörner, Measurement of the Berry curvature of solids using high-harmonic spectroscopy, *Nat. Commun.* **9**, 916 (2018).
- [16] D. Bauer and K. K. Hansen, High-Harmonic Generation in Solids with and without Topological Edge States, *Phys. Rev. Lett.* **120**, 177401 (2018).
- [17] K. K. Hansen, D. Bauer, and L. B. Madsen, Finite-system effects on high-order harmonic generation: From atoms to solids, *Phys. Rev. A* **97**, 0043424 (2018).
- [18] R. E. F. Silva, Á. Jiménez-Galán, B. Amorim, O. Smirnova, and M. Ivanov, Topological strong-field physics on sub-laser-cycle timescale, *Nat. Photonics* **13**, 849 (2019).
- [19] Á. Jiménez-Galán, R. E. F. Silva, O. Smirnova, and M. Ivanov, Lightwave control of topological properties in 2D materials for sub-cycle and non-resonant valley manipulation, *Nat. Photonics* **14**, 728 (2020).
- [20] S. Sederberg, F. Kong, F. Hufnagel, C. Zhang, E. Karimi, and P. B. Corkum, Vectorized optoelectronic control and metrology in a semiconductor, *Nat. Photonics* **14**, 680 (2020).
- [21] I. Grinberg, D. V. West, M. Torres, G. Gou, D. M. Stein, L. Wu, G. Chen, E. M. Gallo, A. R. Akbashev, P. K. Davies, J. E. Spanier, and A. M. Rappe, Perovskite oxides for visible-light-absorbing ferroelectric and photovoltaic materials, *Nature (London)* **503**, 509 (2013).
- [22] L. Z. Tan, F. Zheng, S. M. Young, F. Wang, S. Liu, and A. M. Rappe, Shift current bulk photovoltaic effect in polar materials—hybrid and oxide perovskites and beyond, *npj Comput. Mater.* **2**, 16026 (2016).
- [23] W. Shockley and H. J. Queisser, Detailed balance limit of efficiency of P-n junction solar cells, *J. Appl. Phys.* **32**, 510 (1961).
- [24] R. Atanasov, A. Haché, J. L. P. Hughes, H. M. van Driel, and J. E. Sipe, Coherent Control of Photocurrent Generation in Bulk Semiconductors, *Phys. Rev. Lett.* **76**, 1703 (1996).
- [25] A. Haché, Y. Kostoulas, R. Atanasov, J. L. P. Hughes, J. E. Sipe, and H. M. van Driel, Observation of Coherently Controlled Photocurrent in Unbiased, Bulk GaAs, *Phys. Rev. Lett.* **78**, 306 (1997).
- [26] R. D. R. Bhat and J. E. Sipe, Optically Injected Spin Currents in Semiconductors, *Phys. Rev. Lett.* **85**, 5432 (2000).
- [27] E. Sternemann, T. Jostmeier, C. Ruppert, H. T. Duc, T. Meier, and M. Betz, Femtosecond quantum interference control of electrical currents in GaAs: Signatures beyond the perturbative Chi(3) limit, *Phys. Rev. B* **88**, 165204 (2013).
- [28] D. A. Bas, K. Vargas-Velez, S. Babakiray, T. A. Johnson, P. Borisov, T. D. Stanescu, D. Lederman, and A. D. Bristow, Coherent control of injection currents in high-quality films of Bi<sub>2</sub>Se<sub>3</sub>, *Appl. Phys. Lett.* **106**, 041109 (2015).
- [29] L. Z. Tan and A. M. Rappe, Upper limit on shift current generation in extended systems, *Phys. Rev. B* **100**, 0085102 (2019).
- [30] A. Schiffrin, T. Paasch-Colberg, N. Karpowicz, V. Apalkov, D. Gerster, S. Mühlbrandt, M. Korbman, J. Reichert, M. Schultze, S. Holzner, J. V. Barth, R. Kienberger, R. Ernstorfer, V. S. Yakovlev, M. I. Stockman, and F. Krausz, Optical-field-induced current in dielectrics, *Nature (London)* **493**, 70 (2013).
- [31] M. S. Wismer, S. Y. Kruchinin, M. Ciappina, M. I. Stockman, and V. S. Yakovlev, Strong-Field Resonant Dynamics in Semiconductors, *Phys. Rev. Lett.* **116**, 197401 (2016).
- [32] F. Langer, Y.-P. Liu, Z. Ren, V. Flodgren, C. Guo, J. Vogelsang, S. Mikaelsson, I. Sytcevic, J. Ahrens, A. L'Huillier, C. L. Arnold, and A. Mikkelsen, Few-cycle lightwave-driven currents in a semiconductor at high repetition rate, *Optica* **7**, 276 (2020).
- [33] T. Higuchi, C. Heide, K. Ullmann, H. B. Weber, and P. Hommelhoff, Light-field-driven currents in graphene, *Nature (London)* **550**, 224 (2017).

- [34] C. Heide, T. Higuchi, H. B. Weber, and P. Hommelhoff, Coherent Electron Trajectory Control in Graphene, *Phys. Rev. Lett.* **121**, 207401 (2018).
- [35] C. Heide, T. Boolakee, T. Higuchi, H. B. Weber, and P. Hommelhoff, Interaction of carrier envelope phase-stable laser pulses with graphene: The transition from the weak-field to the strong-field regime, *New J. Phys.* **21**, 045003 (2019).
- [36] C. Heide, T. Boolakee, T. Higuchi, and P. Hommelhoff, Sub-cycle temporal evolution of light-induced electron dynamics in hexagonal 2D materials, *JPhys Photonics* **2**, 024004 (2020).
- [37] See Supplemental Material at <http://link.aps.org/supplemental/10.1103/PhysRevLett.127.126601> for details on the methodology used in calculations as well as some additional results.
- [38] A. Castro, H. Appel, M. Oliveira, C. A. Rozzi, X. Andrade, F. Lorenzen, M. A. L. Marques, E. K. U. Gross, and A. Rubio, Octopus: A tool for the application of time-dependent density functional theory, *Phys. Status Solidi* **243**, 2465 (2006).
- [39] X. Andrade, D. Strubbe, U. De Giovannini, H. Larsen, M. J. T. Oliveira, J. Alberdi-rodriguez, A. Varas, I. Theophilou, N. Helbig, M. J. Verstraete, L. Stella, F. Nogueira, A. Castro, M. A. L. Marques, and A. Rubio, Real-space grids and the octopus code as tools for the development of new simulation approaches for electronic systems, *Phys. Chem. Chem. Phys.* **17**, 31371 (2015).
- [40] N. Tancogne-Dejean *et al.*, Octopus, a computational framework for exploring light-driven phenomena and quantum dynamics in extended and finite systems, *J. Chem. Phys.* **152**, 124119 (2020).
- [41] C. Hartwigsen, S. Goedecker, and J. Hutter, Relativistic separable dual-space Gaussian pseudopotentials from H to Rn, *Phys. Rev. B* **58**, 3641 (1998).
- [42] R. A. Roberts and W. C. Walker, Optical study of the electronic structure of diamond, *Phys. Rev.* **161**, 730 (1967).
- [43] H. Löfås, A. Grigoriev, J. Isberg, and R. Ahuja, Effective masses and electronic structure of diamond including electron correlation effects in first principles calculations using the GW-approximation, *AIP Adv.* **1**, 032139 (2011).
- [44] J. P. Perdew, K. Burke, and M. Ernzerhof, Generalized Gradient Approximation Made Simple, *Phys. Rev. Lett.* **77**, 3865 (1996).
- [45] M. Bernardi, D. Vigil-Fowler, J. Lischner, J. B. Neaton, and S. G. Louie, Ab Initio Study of Hot Carriers in the First Picosecond after Sunlight Absorption in Silicon, *Phys. Rev. Lett.* **112**, 257402 (2014).
- [46] O. Neufeld, D. Podolsky, and O. Cohen, Floquet group theory and its application to selection rules in harmonic generation, *Nat. Commun.* **10**, 405 (2019).
- [47] R. M. Swanson, A vision for crystalline silicon photovoltaics, *Prog. Photovoltaics Res. Appl.* **14**, 443 (2006).
- [48] M. S. Mrudul, Á. Jiménez-Galán, M. Ivanov, and G. Dixit, Light-induced valleytronics in pristine graphene, *Optica* **8**, 422 (2021).
- [49] N. Tancogne-Dejean, O. D. Mücke, F. X. Kärtner, and A. Rubio, Ellipticity dependence of high-harmonic generation in solids originating from coupled intraband and interband dynamics, *Nat. Commun.* **8**, 745 (2017).
- [50] I. Floss, C. Lemell, G. Wachter, V. Smejkal, S. A. Sato, X. M. Tong, K. Yabana, and J. Burgdörfer, Ab initio multiscale simulation of high-order harmonic generation in solids, *Phys. Rev. A* **97**, 011401(R) (2018).
- [51] C. Yu, K. K. Hansen, and L. B. Madsen, High-order harmonic generation in imperfect crystals, *Phys. Rev. A* **99**, 063408 (2019).
- [52] X.-M. Tong and S.-I. Chu, Time-dependent density-functional theory for strong-field multiphoton processes: Application to the study of the role of dynamical electron correlation in multiple high-order harmonic generation, *Phys. Rev. A* **57**, 452 (1998).
- [53] O. Neufeld and O. Cohen, Background-Free Measurement of Ring Currents by Symmetry-Breaking High-Harmonic Spectroscopy, *Phys. Rev. Lett.* **123**, 103202 (2019).
- [54] O. Neufeld and O. Cohen, Probing ultrafast electron correlations in high harmonic generation, *Phys. Rev. Research* **2**, 033037 (2020).
- [55] J. Schoetz, Z. Wang, E. Pisanty, M. Lewenstein, M. F. Kling, and M. F. Ciappina, Perspective on petahertz electronics and attosecond nanoscopy, *ACS Photonics* **6**, 3057 (2019).